

SEP 13 1979

Item 830-H-15

NASA 60: 1525

COMPLETED

NASA Technical Paper 1525

Anisotropic Friction, Deformation,
and Fracture of Single-Crystal
Silicon Carbide at Room Temperature

Kazuhisa Miyoshi and Donald H. Buckley

AUGUST 1979

NASA

24

NASA Technical Paper 1525

Anisotropic Friction, Deformation, and Fracture of Single-Crystal Silicon Carbide at Room Temperature

Kazuhisa Miyoshi and Donald H. Buckley
Lewis Research Center
Cleveland, Ohio



National Aeronautics
and Space Administration

Scientific and Technical
Information Branch

1979

SUMMARY

The anisotropic friction, deformation, and fracture of the $\{0001\}$, $\{10\bar{1}0\}$, and $\{11\bar{2}0\}$ silicon carbide surfaces were investigated. Sliding friction experiments were conducted with a diamond rider sliding on the $\{0001\}$ surface in the $\langle 10\bar{1}0 \rangle$ and $\langle 11\bar{2}0 \rangle$ directions, on the $\{10\bar{1}0\}$ surface in the $\langle 0001 \rangle$ and $\langle 11\bar{2}0 \rangle$ directions, and on the $\{11\bar{2}0\}$ surface in the $\langle 0001 \rangle$ and $\langle 10\bar{1}0 \rangle$ directions. The experiments were conducted with loads of 0.1, 0.2, and 0.3 newton, at a sliding velocity of 3 millimeters per minute both in mineral oil and in dry argon at room temperature. The silicon carbide was subjected to single-pass sliding and the sliding distance was 1 to 2 millimeters.

The $\langle 10\bar{1}0 \rangle$ direction on the basal $\{0001\}$ plane exhibits the lowest coefficient of friction and the greatest resistance to abrasion for silicon carbide. The anisotropic friction and deformation of the $\{0001\}$, $\{10\bar{1}0\}$, and $\{11\bar{2}0\}$ silicon carbide surfaces are primarily controlled by the slip system $\{10\bar{1}0\} \langle 11\bar{2}0 \rangle$. The anisotropic fracture during sliding on the basal $\{0001\}$ plane is due to surface cracking along $\{10\bar{1}0\}$ and subsurface cracking along $\{0001\}$. The fracture during sliding on the $\{10\bar{1}0\}$ and $\{11\bar{2}0\}$ surfaces is due to surface cracking along $\{0001\}$ and $\{11\bar{2}0\}$ or $\{10\bar{1}0\}$, and subsurface cracking along $\{10\bar{1}0\}$.

INTRODUCTION

Silicon carbide is used in thousands of industrial grinding operations today. Moreover, it is expected to be one of the future's most desirable materials for such uses as grinding wheels; turbine blades, vanes, and shrouds in gas turbine engines; and first-wall materials in controlled thermonuclear reactors.

The present authors have conducted a series of experimental studies to determine the tribophysical properties of single-crystal silicon carbide (refs. 1 to 6). One of the examinations of single-crystal silicon carbide in sliding contact with a diamond rider revealed that the friction, deformation, and fracture of the silicon carbide $\{0001\}$ surface depends on the crystallographic orientation and that the anisotropies are primarily controlled by the slip system $\{10\bar{1}0\} \langle 11\bar{2}0 \rangle$ and cleavages of $\{10\bar{1}0\}$ and $\{0001\}$ (ref. 1). It would be of further interest to know the friction, deformation, and fracture behavior of the silicon carbide $\{10\bar{1}0\}$ and $\{11\bar{2}0\}$ surfaces. Knowing the influence of crystallographic orientation on the friction, deformation, and fracture behavior of silicon carbide may assist us in improving its abrasion-resistance. The

wear of abrasives such as silicon carbide occurs in such operations as grinding, and it is highly desirable to minimize this wear.

In the study discussed herein the friction, deformation, and fracture behavior of single-crystal silicon carbide $\{0001\}$, $\{10\bar{1}0\}$, and $\{11\bar{2}0\}$ surfaces in contact with a diamond rider were examined. The orientation of silicon carbide and its effect on these properties were also examined.

MATERIALS

The single-crystal silicon carbide platelets used in these experiments were of a 99.9-percent pure compound of silicon and carbon. Silicon carbide has a hexagonal close-packed crystal structure with the most commonly occurring unit cell dimensions of $a = 3.0817 \text{ \AA}$ and $c = 15.1183 \text{ \AA}$ (table I). The hardness data, slip systems, and cleavage planes of single-crystal silicon carbide have been reported and are presented in table I (refs. 7 to 13).

The diamonds were commercially purchased. Diamond, the hardest known material (ref. 14), indents silicon carbide without itself suffering permanent deformation. Its elastic constants are also very high. The Young's modulus of silicon carbide, is about 4.5×10^5 pascals (ref. 15), while that of diamond lies between 7×10^5 and 10×10^5 pascals (ref. 16).

APPARATUS

The apparatus used in this investigation was a system capable of applying load and measuring friction in mineral oil and in argon at atmospheric pressure. The mechanism for measuring friction is shown schematically in figure 1. The beam contains one flat, which has been machined normal to the direction of friction application. The end of the rod contains the diamond rider. The load is applied by placing dead weights on a pan on top of the rod. Under an applied load the friction force is sensed by strain gages.

EXPERIMENTAL PROCEDURE

The single-crystal silicon carbide surfaces were mechanically polished with 3-micrometer diamond powder and then 1-micrometer aluminum oxide (Al_2O_3) powder. The silicon carbide flat specimen surfaces were oriented such that the $\{0001\}$, $\{10\bar{1}0\}$, or $\{11\bar{2}0\}$ plane was nearly parallel to the sliding interface (see fig. 2). The orienta-

tions of the silicon carbide $\{0001\}$ and the other two planes are to an accuracy $\pm 2^\circ$.

The diamond riders were approximately conical (as shown in fig. 3). However, the tip of rider is a four-sided regular pyramid, having round edges and a round apex. The apical angle was about 120° , and the radius of curvature at the apex was less than 5 micrometers. The riders were polished with Al_2O_3 powder before each friction experiment. Both the silicon carbide and diamond surfaces were rinsed with water and 200-proof ethyl alcohol before use. The single-pass friction experiments were conducted with a total sliding distance of 1 to 2 millimeters at a sliding velocity of 3 millimeters per minute. They were conducted in degassed mineral oil and in dry argon at atmospheric pressure and room temperature. Typical properties of the mineral oil appear in table II.

The sliding reported herein involved mostly plastic flow and local surface cracking in silicon carbide. In the present experiments, the contact area of the rider sliding on silicon carbide at loads of 0.1, 0.2, and 0.3 newton is approximately the portion of round apex of the rider. Therefore, the widths of the permanent grooves D , as defined in figure 4, were obtained by averaging measurements of 20 samples from 7 to 10 scanning electron micrographs. The specimen surfaces are the correct distance from the beam pivot point in the scanning electron microscope. The accelerating voltage was 18 kilovolts. A 1000-mesh gold grid was used as the standard.

The contact pressure P during sliding may then be defined by $P = W/A$, where W is the applied normal load and A is the horizontal projected area of contact and is given by $A = \pi D^2/8$ (only the front half of the rider is in contact with the flat specimen).

The friction traces presented herein are primarily characterized by a continuous, marked stick-slip behavior. The coefficient of friction is the average, maximum peak height in the friction trace.

RESULTS AND DISCUSSION

Anisotropic Friction and Deformation

Sliding friction experiments were conducted with a diamond rider in contact with flat silicon carbide $\{0001\}$, $\{10\bar{1}0\}$, and $\{11\bar{2}0\}$ surfaces in mineral oil at atmospheric pressure. The sliding generally involves plastic flow and surface cracking. Surface cracking will be discussed in succeeding sections. Figure 5 reveals a typical plastically deformed groove and small wear debris particles which were generated during sliding of the rider.

The basic concept of deformation of silicon carbide is expressed in the scheme of figure 6. Below the rider the material behaves as an outwardly expanding "core"

exerting a uniform hydrostatic pressure on its surroundings. The core is an ideally plastic region within which full plastic yielding occurs. Beyond the plastic yielding lies the elastic "matrix." At the elastic-plastic boundary elastic and plastic strains are of comparable magnitude. The mean pressure increases from the onset of plastic deformation to a fully plastic state.

The coefficient of friction and the width of the permanent groove, involving plastic flow and surface cracking, were measured as functions of crystallographic direction of sliding on the $\{0001\}$, $\{10\bar{1}0\}$, and $\{11\bar{2}0\}$ planes of silicon carbide for the diamond rider in mineral oil. The widths of the permanent grooves were obtained by average measurements of 20 samples from 7 to 10 scanning electron micrographs. The results presented in figure 7 indicate that the coefficient of friction and the groove width are influenced by the crystallographic orientation. The $\langle 11\bar{2}0 \rangle$ direction on the basal $\{0001\}$ plane has the larger groove, primarily resulting from plastic flow and is the direction of high friction for this plane (ref. 1). The $\langle 0001 \rangle$ directions on the $\{10\bar{1}0\}$ and $\{11\bar{2}0\}$ planes have the greater groove width and are the directions of high friction when compared with $\langle 11\bar{2}0 \rangle$ on $\{10\bar{1}0\}$ and $\langle 10\bar{1}0 \rangle$ on the $\{11\bar{2}0\}$. The anisotropies of friction are $\mu \langle 11\bar{2}0 \rangle / \mu \langle 10\bar{1}0 \rangle = 1.2$ on $\{0001\}$, $\mu \langle 0001 \rangle / \mu \langle 11\bar{2}0 \rangle = 1.3$ on $\{10\bar{1}0\}$, and $\mu \langle 0001 \rangle / \mu \langle 10\bar{1}0 \rangle = 1.3$ on $\{11\bar{2}0\}$. The standard deviations in the friction and in the widths of the permanent grooves with repeated experiments were about 5 percent of those indicated in the figure.

Figure 8 represents the contact pressure calculated from the data of the groove width in figure 7 and the Knoop hardness obtained by Shaffer (ref. 9). The anisotropies of the contact pressure during sliding and the Knoop hardness clearly correlate with each other.

Several slip systems have been observed in hexagonal silicon carbide, such as $\{0001\} \langle 11\bar{2}0 \rangle$, $\{3\bar{3}01\} \langle 11\bar{2}0 \rangle$, and $\{10\bar{1}0\} \langle 11\bar{2}0 \rangle$ (refs. 10 and 11). The present authors have already shown that the $\{10\bar{1}0\} \langle 11\bar{2}0 \rangle$ slip system observed on the sliding surface was responsible for the anisotropic friction and deformation behavior of silicon carbide during sliding in the $\langle 10\bar{1}0 \rangle$ and $\langle 11\bar{2}0 \rangle$ directions on a $\{0001\}$ silicon carbide surface. The experimental results (ref. 1) generally agreed with Daniel and Dunn's (ref. 17) resolved shear stress analysis based on the slip system $\{10\bar{1}0\} \langle 11\bar{2}0 \rangle$. The minima and maxima of the resolved shear stress for the $\{0001\}$ plane of hexagonal crystal match the hard and soft directions on that plane, that is, the $\langle 10\bar{1}0 \rangle$ and $\langle 11\bar{2}0 \rangle$ directions, respectively. But the experimental results could not explain Brookes, O'Neill, and Redfern's (ref. 11) resolved shear stress analysis based on the $\{0001\} \langle 11\bar{2}0 \rangle$ slip system. Thus, the anisotropies of friction and hardness on the $\{0001\}$ plane strongly correlate with the resolved shear stress, based on the slip system $\{10\bar{1}0\} \langle 11\bar{2}0 \rangle$.

The anisotropies of friction, contact pressure (groove width), and Knoop hardness on the $\{10\bar{1}0\}$ and $\{11\bar{2}0\}$ planes were correlated with reference 17's resolved shear stress based on the $\{10\bar{1}0\} \langle 0001 \rangle$ and $\{10\bar{1}0\} \langle 11\bar{2}0 \rangle$ slip systems. They were also correlated with reference 11's resolved shear stress based on the $\{1\bar{2}10\} \langle 10\bar{1}0 \rangle$ slip system. However, the slip system actually observed in hexagonal silicon carbide, the $\{10\bar{1}0\} \langle 11\bar{2}0 \rangle$ slip system, may be responsible for those anisotropies on the $\{10\bar{1}0\}$ and $\{11\bar{2}0\}$ planes.

Similar data for Knoop hardness anisotropy of tungsten carbide $\{0001\}$ and $\{10\bar{1}0\}$ surfaces have been reported by French and Thomas (ref. 18) who used a resolved shear-stress calculation involving the $\{10\bar{1}0\} \langle 0001 \rangle$ and $\{10\bar{1}0\} \langle 11\bar{2}0 \rangle$ slip systems to explain the data. Thus, the anisotropies of friction, contact pressure, and Knoop hardness on the $\{0001\}$, $\{10\bar{1}0\}$, and $\{11\bar{2}0\}$ planes of silicon carbide are primarily controlled by the slip system $\{10\bar{1}0\} \langle 11\bar{2}0 \rangle$.

Figures 7 and 8 suggest that the $\langle 10\bar{1}0 \rangle$ on the basal plane of silicon carbide would exhibit the lowest coefficient of friction and greatest resistance to abrasion resulting from plastic deformation.

Influence of Environment on Friction

Sliding friction experiments were conducted with a diamond rider in contact with a flat silicon carbide $\{0001\}$ surface in mineral oil and in dry argon at atmospheric pressure. Sliding generally involves plastic flow and surface cracking, as already mentioned. The coefficients of friction were measured as functions of crystallographic orientation of sliding on the basal $\{0001\}$ plane of silicon carbide. All friction traces measured at a load of 0.2 newton are characterized by a continuous stick-slip behavior. Figure 9, which presents the coefficients of friction at the load of 0.2 newton, reveals that the coefficient of friction depends (1) on the environment and (2) on the crystallographic orientation of silicon carbide. In an argon atmosphere, that is, in the condition of dry friction, the coefficients of friction and anisotropy of friction ($K\{0001\} = \mu \langle 11\bar{2}0 \rangle / \mu \langle 10\bar{1}0 \rangle$) are higher than in mineral oil. Observation of the wear track confirmed that the surface cracking during sliding of the rider in argon was generally much greater than that in oil.

The friction is due to shearing at the interface and plowing of bulk silicon carbide. The use of oil, which minimizes the shear strength at the interface, influences the coefficient of friction, anisotropy of friction, and surface cracking.

Anisotropic Fracture

As mentioned in the previous sections, the sliding of the diamond rider produces both plastic deformation and cracking or fracture in silicon carbide.

The surface crack patterns surrounding the permanent grooves made by rider were of three types, as schematically indicated by P, S, and L in figure 10. Crack P is very small, is in the groove, and propagates perpendicular to the sliding direction. Crack S is primarily on both sides of the groove and propagates outward from the groove. Crack L propagates parallel to the sliding direction, that is, along the sliding direction in the central portion of the groove. The geometries of cracks P and L are generally independent of the crystallographic orientation. As cracks L are mostly covered with a plastic deformed layer, they cannot be observed without etching or cross-sectioning the groove.

From reference 19 the initiation of each crack and the crack geometry may be determined by the maxima in tensile stresses in the contact zone or surrounding groove. It seems reasonable that cracks will tend to initiate at one of these favored locations.

Surface cracks S start from maxima tensile stress fields (ref. 19). However, the propagation of these cracks depends on the crystallographic orientation.

All surface cracks propagate in the subsurface, as schematically indicated in figures 10(b) and (c), which summarize lateral and longitudinal cross-sectional views of the groove.

In the lateral cross section, the cracks S and L appear to propagate in the subsurface and straight downward (at a nearly right angle to the specimen surface). These cracks continue to extend out of the primary plane. In some instances, however, crack diversion will occur along a weak plane in silicon carbide (e. g., the basal or prismatic plane). Thus, subsurface crack growth may occur by secondary fracture mechanisms.

Figures 11(a) and (b), lateral cross-section views through a groove in silicon carbide, tend to confirm our speculations on the geometries of the cracks. Crack L has grown straight downward along the contact axis of the rider underneath the groove. Figure 11(b) also indicates that crack S has grown straight downward (primary crack) and that the tip of crack under the surface becomes curved and propagates along the secondary weak plane (secondary crack B), that is, the basal plane. The crack then propagates parallel to the sliding interface of the specimen.

In the longitudinal cross-section view (fig. 10(c)), crack P appears to propagate subsurface. Cracks P curve during crack propagation as do cracks L and S. The tips of the cracks propagate along the secondary weak plane, that is, the basal plane parallel to the sliding surface of the specimen. Figures 12(a) and (b) are the longitudinal cross-sectional views through a groove of silicon carbide. They confirm our speculations on the geometries of cracks P, S, and secondary crack B. The crack S has grown straight downward, and the tips of the cracks have curved and propagated along the basal plane (fig. 11(a)). Figure 12(b) also shows the result of cracks P and

the secondary cracks B being generated, propagating, and then intersecting - the cause of the fracturing of the silicon carbide surface.

The gross fracturing of silicon carbide during sliding in the $\langle 10\bar{1}0 \rangle$ and $\langle 11\bar{2}0 \rangle$ directions on the $\{0001\}$ surface was primarily due to surface cracking of the $\{10\bar{1}0\}$ plane and subsurface cracking of the $\{0001\}$ plane (ref. 1).

Figures 13 to 15 show scanning electron micrographs of the grooves on the silicon carbide $\{10\bar{1}0\}$ and $\{11\bar{2}0\}$ surfaces generated by a single pass of the diamond rider. In figures 13 and 14 the rectangular area consists of a large crack with lodged wear debris, where the cracks were generated, propagated, and then intersected during sliding of the rider. The cracking generally depends on the crystallographic orientation. The surface cracks propagate primarily in the $\langle 0001 \rangle$ and $\langle 11\bar{2}0 \rangle$ or $\langle 10\bar{1}0 \rangle$ directions. The formations of these cracks are due to the surface-cleavage cracking along planes $\{0001\}$ and $\{11\bar{2}0\}$ or $\{10\bar{1}0\}$, respectively. It is anticipated from figures 12 and 13 that subsurface cracking also occurs underneath the lodged rectangular wear debris.

Figure 15 reveals a gross fracture pit where the gross wear debris particle has already been ejected. The fracture pit reveals that the fracturing is the result of surface cracking along primary cleavage planes $\{10\bar{1}0\}$ and $\{0001\}$ and subsurface cracking along $\{10\bar{1}0\}$, as anticipated. In the figure 15 sharp edges zig-zag along cleavage planes $\{10\bar{1}0\}$ and $\{0001\}$. The bottom surface of the fracture pit is parallel to the sliding surface.

Thus, again the fracture of silicon carbide during sliding on the $\{10\bar{1}0\}$ and $\{11\bar{2}0\}$ surfaces in various directions (such as $\langle 0001 \rangle$, $\langle 10\bar{1}0 \rangle$, or $\langle 11\bar{2}0 \rangle$) may be explained in terms of the fracture energy acting in the $\{10\bar{1}0\}$, $\{11\bar{2}0\}$, and $\{0001\}$ cleavage systems.

CONCLUSIONS

The following conclusions are drawn from this study of silicon carbide surfaces after sliding contact with diamond:

1. The $\langle 10\bar{1}0 \rangle$ direction on the basal $\{0001\}$ plane of silicon carbide exhibits the lowest coefficient of friction and the greatest resistance to abrasion.
2. Anisotropic friction and deformation on the $\{0001\}$, $\{10\bar{1}0\}$, and $\{11\bar{2}0\}$ silicon carbide surfaces are primarily controlled by the slip system $\{10\bar{1}0\} \langle 11\bar{2}0 \rangle$.
3. The anisotropic fracture during sliding on the basal plane is due to surface cracking along $\{10\bar{1}0\}$ and subsurface cracking along $\{0001\}$. The fracture during sliding on the $\{10\bar{1}0\}$ and $\{11\bar{2}0\}$ surfaces is due to surface cracking along $\{0001\}$ and $\{11\bar{2}0\}$ or $\{10\bar{1}0\}$ and to subsurface cracking along $\{10\bar{1}0\}$.

4. The surface crack patterns surrounding plastic grooves are of three types. One is characterized by a crack propagating perpendicular to the sliding direction. The second is a crack propagating parallel to the sliding direction. The geometries of these cracks are generally independent of the crystallographic orientation and depend on the maxima tensile stress fields. The third is a surface crack that propagates in, that is to say it is dependent on the crystallographic orientation.

5. All surface cracks extend from the primary plane into the subsurface. In some cracks, however, diversion of the crack occurs along weak cleavage planes in the subsurface. This diversion constitutes secondary fracture growth in the subsurface.

Lewis Research Center,

National Aeronautics and Space Administration,

Cleveland, Ohio, May 16, 1979,

506-16.

REFERENCES

1. Miyoshi, K.; and Buckley, D. H.: Friction and Deformation Behavior of Single-Crystal Silicon Carbide. NASA TP-1053, 1977.
2. Miyoshi, K.; and Buckley, D. H.: Friction and Wear Behavior of Single-Crystal Silicon Carbide in Contact with Titanium. NASA TP-1035, 1977.
3. Miyoshi, K.; and Buckley, D. H.: Friction and Metal Transfer for Single-Crystal Silicon Carbide in Contact with Various Metals in Vacuum. NASA TP-1191, 1978.
4. Miyoshi, K.; and Buckley, D. H.: Wear of Single-Crystal Silicon Carbide in Contact with Various Metals in Vacuum. NASA TP-1198, 1978.
5. Miyoshi, K.; and Buckley, D. H.: Effect of Oxygen and Nitrogen Interactions on Friction of Single-Crystal Silicon Carbide. NASA TP-1265, 1978.
6. Miyoshi, K.; and Buckley, D. H.: Friction and Wear of Metals with a Single-Crystal Abrasive Grit of Silicon Carbide - Effect of Shear Strength of Metal. NASA TP-1293, 1978.
7. Taylor, A.; and Laidler, D. S.: The Formation and Crystal Structure of Silicon Carbide. Brit. J. Appl. Phys., vol. 7, July 1950, pp. 174-181.
8. Shaffer, P. T. B.: A Review of the Structure of Silicon Carbide. Acta Crystallogr., Sect. B, vol. 25, 1969, pp. 477-488.
9. Shaffer, Peter T. B.: Effect of Crystal Orientation on Hardness of Silicon Carbide. J. Am. Ceram. Soc., vol. 47, no. 9, Sep. 1964, p. 466.

10. Amelinckx, S.; Strumane, G.; and Webb, W. W.: Dislocations in Silicon Carbide. *J. Appl. Phys.*, vol. 31, no. 8, Aug. 1960.
11. Keyes, R. W.: Morphology of Commercial Silicon Carbide Crystals. *Silicon Carbide: A High Temperature Semiconductor*, J. R. O'Connor and J. Smiltens, eds., Pergamon Press, Inc., 1960, pp. 217-220.
12. Venkateswaran, C. S.: The Dynamic X-ray Reflections in Carbon Silicide. *Proc. Indian Acad. Sci., Ser. A*, vol. 28, Nov. 1948, pp. 316-323.
13. Brookes, C. A.; O'Neill, J. B.; and Redfern, B. A. W.: Anisotropy in the Hardness of Single Crystals. *Proc. Roy. Soc. (London)*, Ser. A, vol. 322, no. 1548, Mar. 1971, pp. 73-88.
14. Bowden, F. P.; and Tabor, D.: *The Friction and Lubrication of Solids. Part II.* Clarendon Press (London), 1964.
15. Hasselman, D. P. H.; and Batha, H. D.: Strength of Single Crystal Silicon Carbide. *Appl. Phys. Lett.*, vol. 2, no. 3, Mar. 15, 1963, pp. 111-113.
16. Bhagavantam, S.; and Bhimasenachari, J.: Elastic Constants of Diamond. *Proc. Roy. Soc. (London)*, Ser. A, vol. 187, no. 1010, Nov. 5, 1946, pp. 381-384.
17. Daniels, F. W.; and Dunn, C. G.: The Effect of Orientation on Knoop Hardness of Single Crystals of Zinc and Silicon Ferrite. *Trans., Am. Soc. Metals*, vol. 41, 1949, pp. 419-442.
18. French, D. N.; and Thomas, D. A.: Hardness Anisotropy and Slip in WC Crystals. *Trans. AIME*, vol. 233, May 1965, pp. 950-952.
19. Lawn, B. R.: Partial Cone Crack Formation in a Brittle Material Loaded with a Sliding Spherical Indenter. *Proc. Roy. Soc. (London)*, Ser. A, vol. 299, no. 1458, 11 July 1967, pp. 307-316.

TABLE I. - PROPERTIES OF SINGLE-CRYSTAL SILICON CARBIDE

[Crystal structure: hexagonal close packed.]

(a) Interatomic distance

Interatomic distance, Å		Lattice ratio, c/a	Source
a	c		
3.0817	15.1183	4.9058	Ref. 7
3.073	15.079	4.9069	Ref. 8

(b) Hardness data

Slip plane	Slip direction	Knoop hardness number ^a
{0001}	$\langle 11\bar{2}0 \rangle$	2917
	$\langle 10\bar{1}0 \rangle$	2954
{10 $\bar{1}0$ }	$\langle 0001 \rangle$	2129
	^b $\langle 0001 \rangle$	2755
{11 $\bar{2}0$ }	$\langle 0001 \rangle$	2391
	^b $\langle 0001 \rangle$	2755

(c) Slip and cleavage systems

Slip plane	Slip direction	Cleavage plane
^d {0001}	^d $\langle 11\bar{2}0 \rangle$	^e {10 $\bar{1}0$ }
^d {3301}	^d $\langle 11\bar{2}0 \rangle$	^e {0001}
^{g, b} {10 $\bar{1}0$ }	^{g, b} $\langle 11\bar{2}0 \rangle$	^g {11 $\bar{2}0$ }

^aLoad, 100 g.^bRef. 9.^cPerpendicular.^dRef. 10.^eRef. 11.^fRef. 12.^gRef. 13.TABLE II. - NAPHTHENIC MINERAL
OIL PROPERTIES^a

Viscosity, m ² /sec (cS):	
At 38 ^o C.	73.4×10 ⁻⁶ (73.4)
At 99 ^o C.	8.35×10 ⁻⁶ (8.35)
Specific gravity:	
At 16 ^o C.	0.880
At 25 ^o C.	0.875
Four point, ^o C	-18
Flashpoint, ^o C	224

^aManufacturer's analysis.

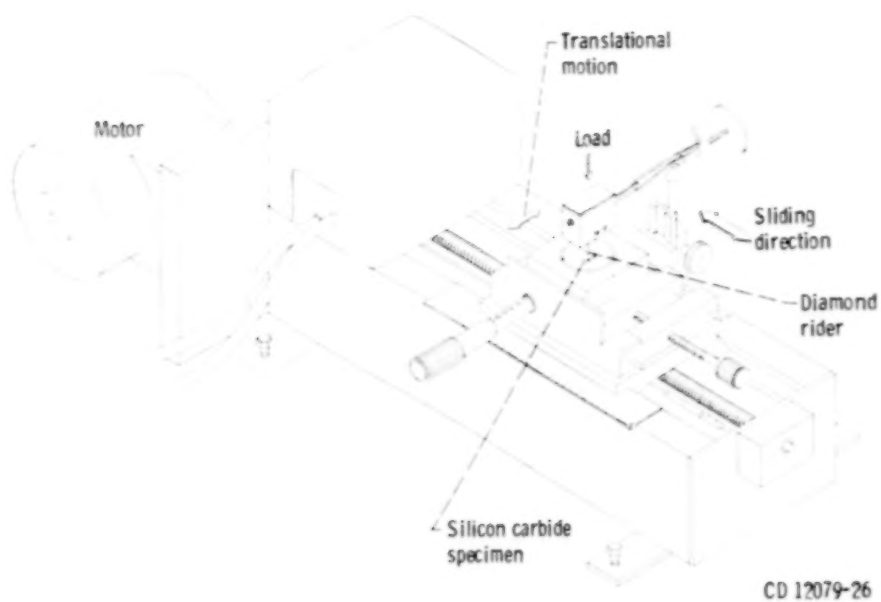


Figure 1. - Friction and wear apparatus.

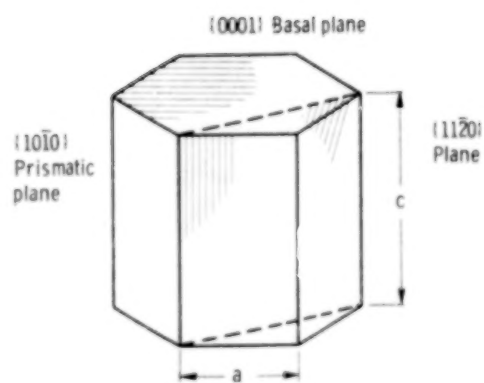


Figure 2. - Hexagonal crystal.

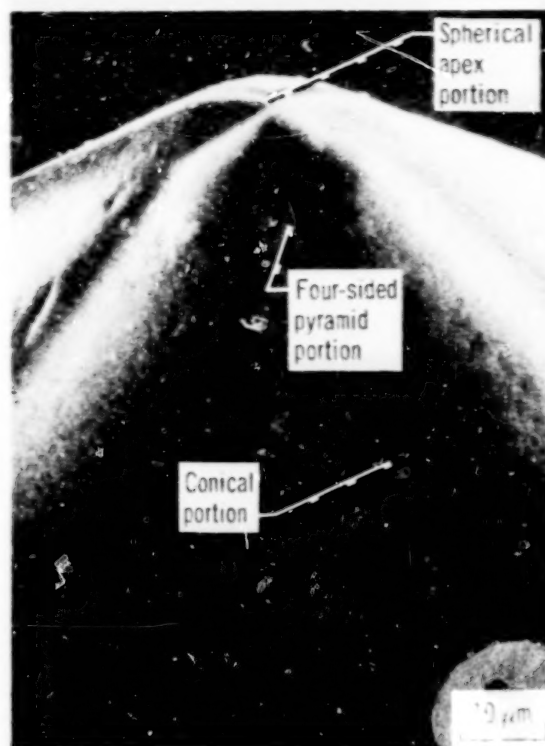


Figure 3. - A diamond rider in the form of four-sided regular pyramid. Apical angle, 120° , radius of apex, $5\ \mu\text{m}$.

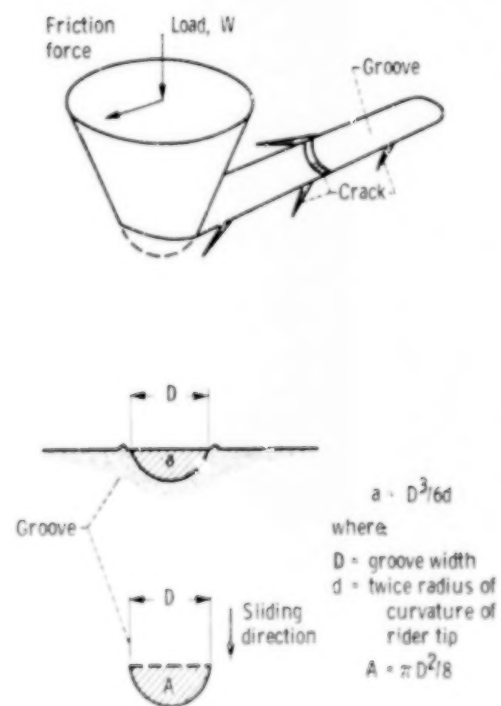
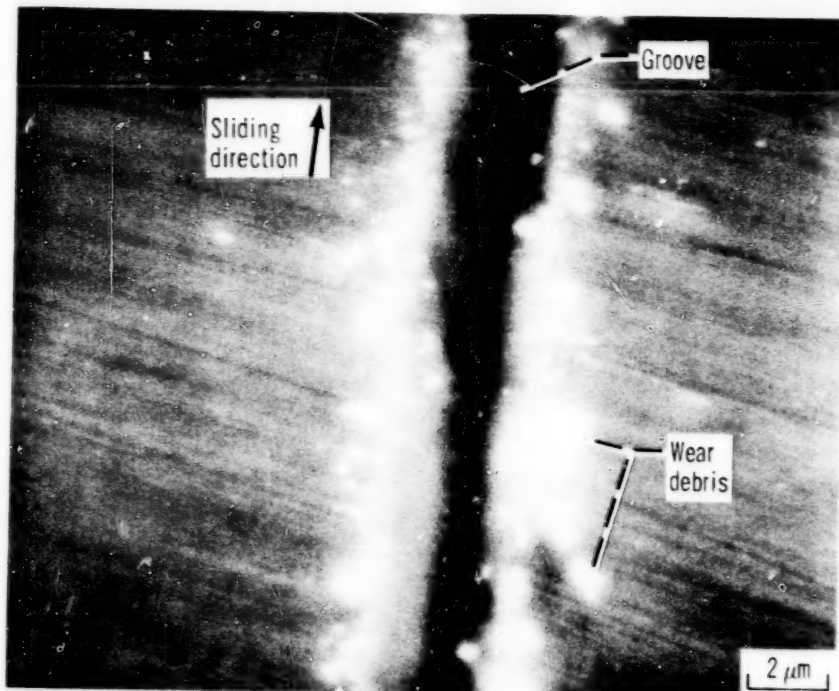
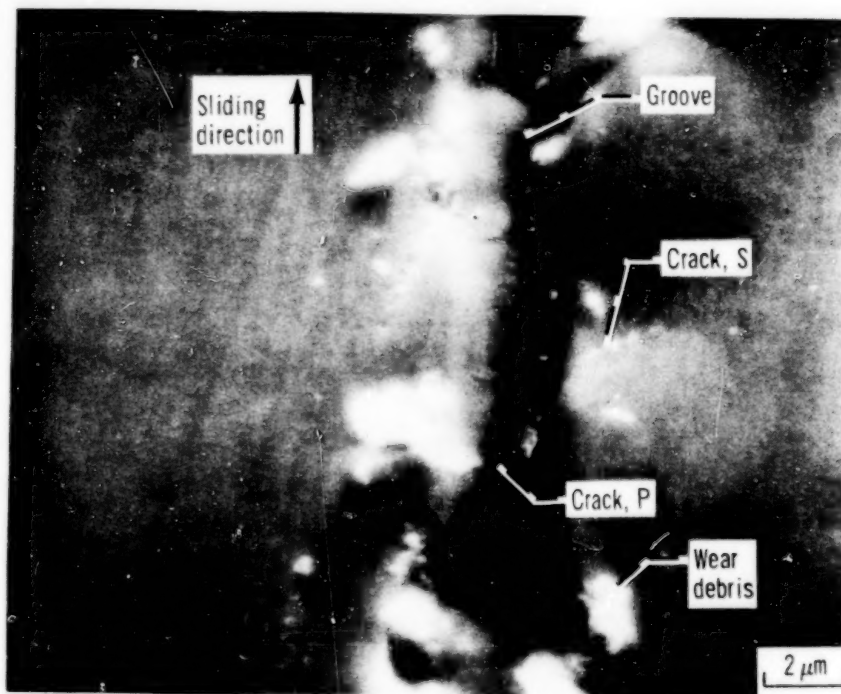


Figure 4. - Schematic diagram of rider contact during sliding.



(a) Groove formed during sliding in $\langle 0001 \rangle$ direction on $\{11\bar{2}0\}$ surface.



(b) Groove formed during sliding in $\langle 10\bar{1}0 \rangle$ direction on $\{11\bar{2}0\}$ surface.

Figure 5. - Scanning electron micrographs of grooves on silicon carbide $\{11\bar{2}0\}$ surface.
Load, 0.2 N; in oil.

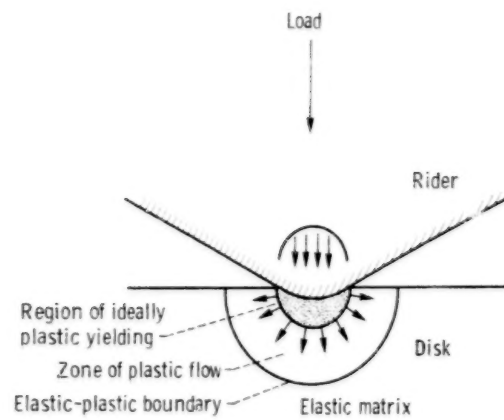


Figure 6. - Model for groove produced by rider.

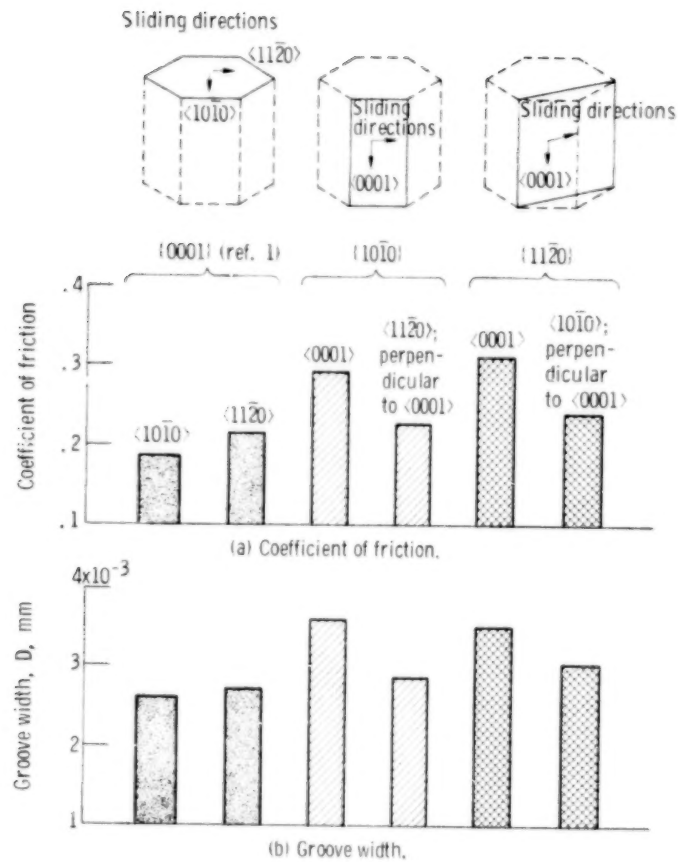


Figure 7 - Coefficients of friction and groove width anisotropies for diamond rider sliding on $\{0001\}$, $\{10\bar{1}0\}$, and $\{11\bar{2}0\}$ silicon carbide surfaces in mineral oil. Load, 0.2 N.

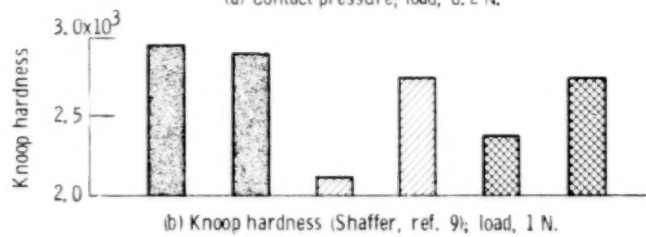
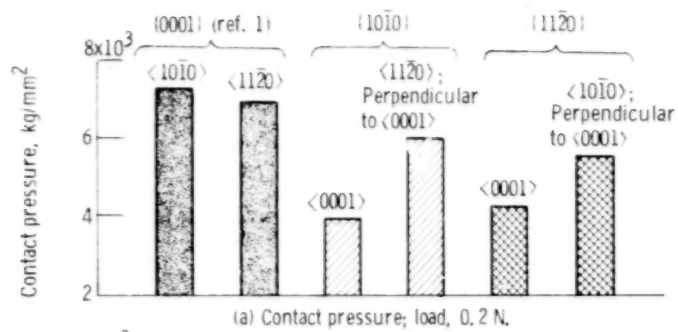


Figure 8. - Contact pressure and Knoop hardness anisotropies on {0001}, {1010}, and {1120} silicon carbide surfaces.

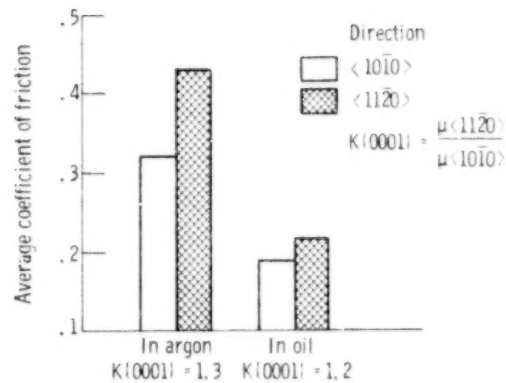
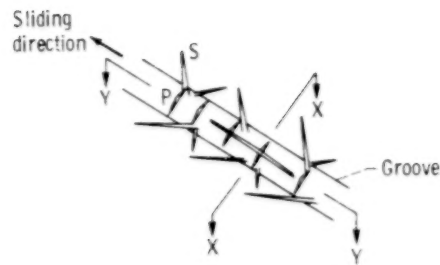


Figure 9. - Friction anisotropy for diamond rider sliding on single-crystal silicon carbide {0001} surface in argon and in oil at atmospheric pressure. Sliding velocity, 3 mm/min; load, 0.2 N; room temperature.



(a) Surface cracks, wear track, and arrangement of cross section.

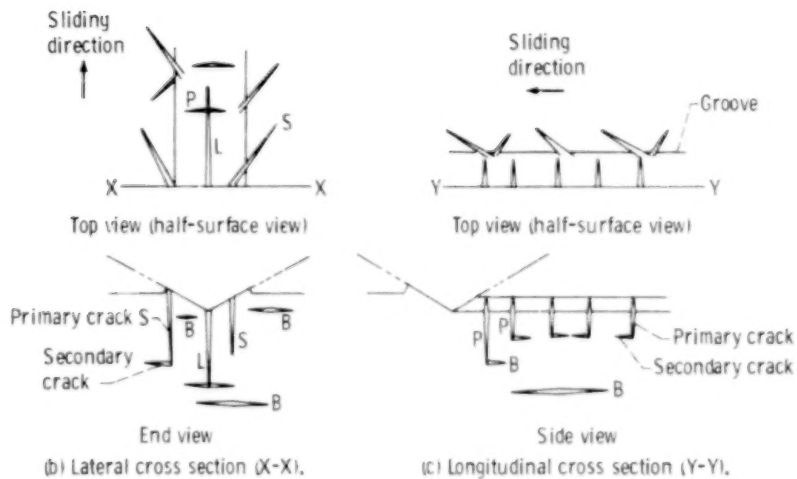
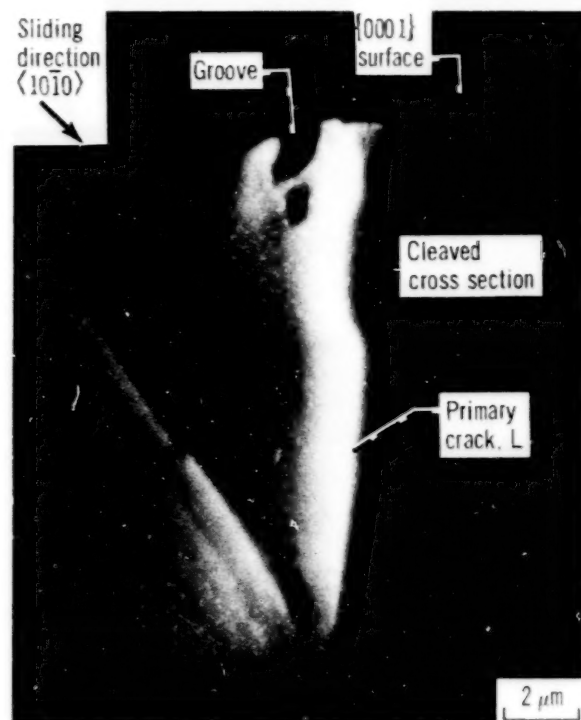
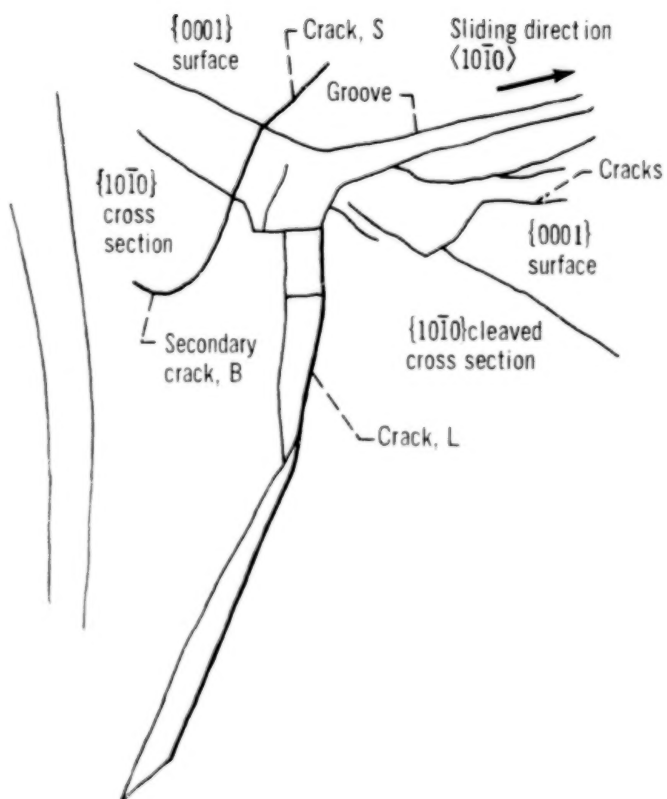


Figure 10. - Schematic model of surface and subsurface cracking during sliding. P: cracks propagating perpendicular to the sliding direction. S: cracks propagating outward from the groove. L: cracks propagating parallel to the sliding direction in the groove. B: cracks generated and propagating in subsurface.

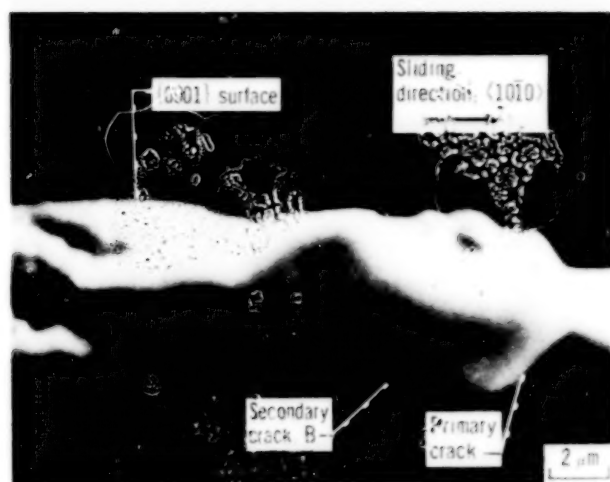


(a) Crack L in subsurface. Load, 0.1 N.

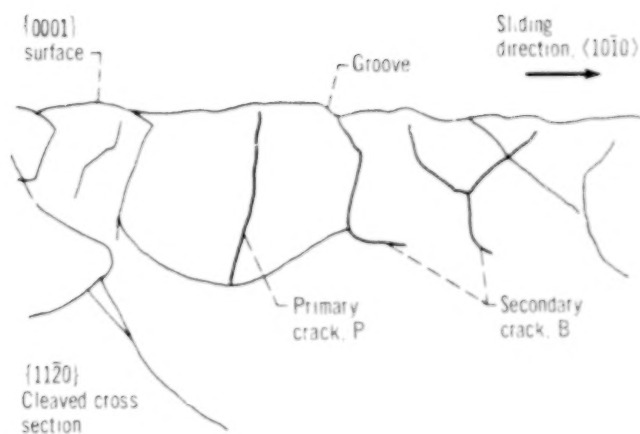


(b) Cracks L and S in subsurface. Load, 0.3 N.

Figure 11. Scanning electron micrographs of grooves on {0001} silicon carbide surfaces. Lateral cross section views of {1010} plane.

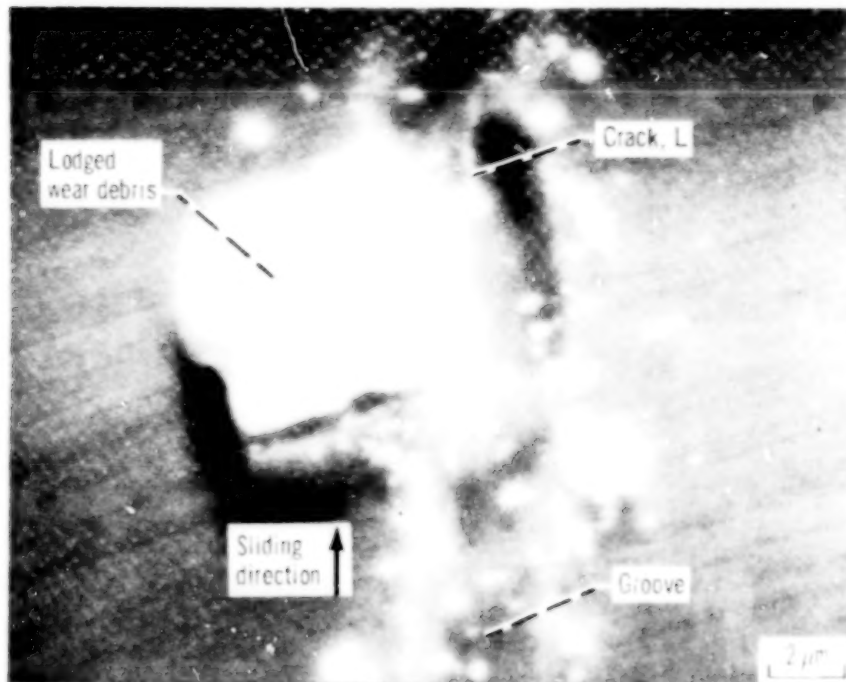


(a) Surface and secondary subsurface crack. Load, 0.3 N.

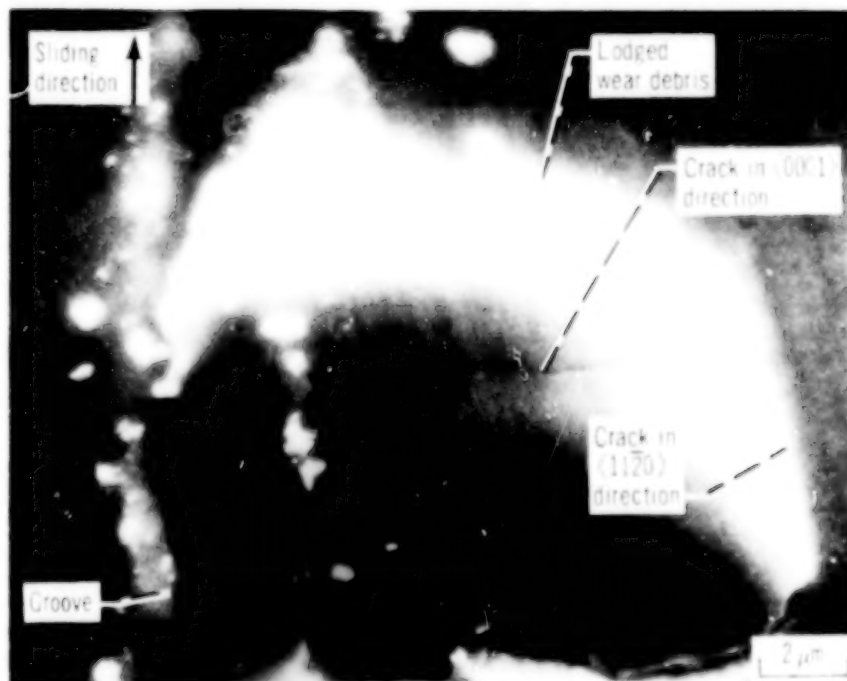


(b) Surface and secondary subsurface cracks. Load, 0.3 N.

Figure 12. - Scanning electron micrographs of grooves on {0001} silicon carbide surfaces. Longitudinal cross section of {1120} plane.



(a) After sliding in $\langle 0001 \rangle$ direction.



(b) After sliding in $\langle 11\bar{2}0 \rangle$ direction

Figure 13 - Scanning electron micrographs of grooves on $\{10\bar{1}0\}$ silicon carbide surfaces.
Load, 0.2 N; in oil



(a) After sliding in (001) direction



(b) After sliding in (110) direction

Figure 14. Scanning electron micrographs of grooves in Ti-6Al-4V after sliding in oil. Load 0.1 N , in oil.

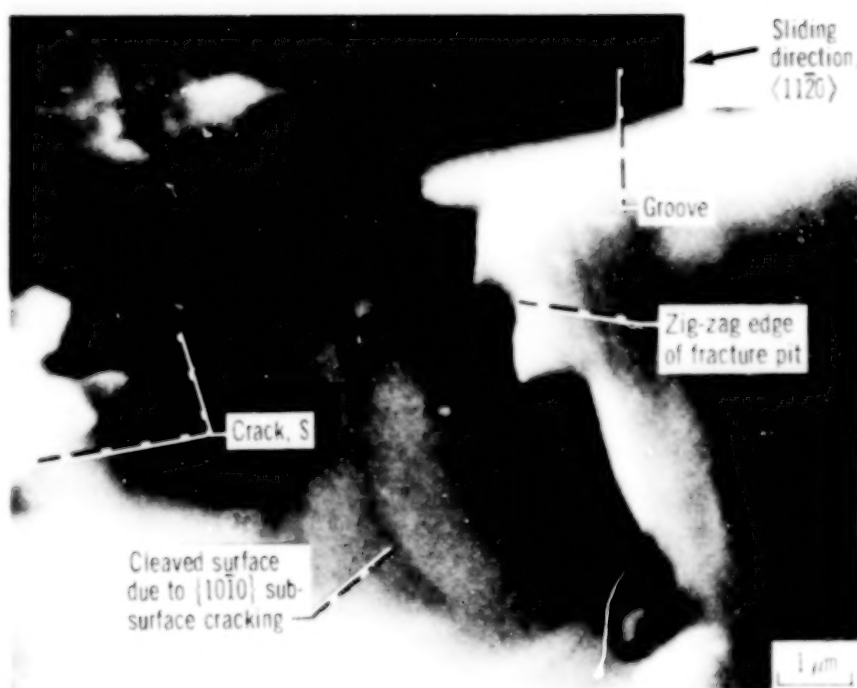


Figure 15. - Scanning electron micrograph of groove on $\{10\bar{1}0\}$ silicon carbide surface.
Load, 0.2 N, in oil.

1. Report No. NASA TP-1525		2. Government Accession No.		3. Recipient's Catalog No.	
4. Title and Subtitle ANISOTROPIC FRICTION, DEFORMATION, AND FRACTURE OF SINGLE-CRYSTAL SILICON CARBIDE AT ROOM TEMPERATURE				5. Report Date August 1979	
				6. Performing Organization Code	
7. Author(s) Kazuhisa Miyoshi and Donald H. Buckley				8. Performing Organization Report No. E-9988	
9. Performing Organization Name and Address National Aeronautics and Space Administration Lewis Research Center Cleveland, Ohio 44135				10. Work Unit No. 506-16	
				11. Contract or Grant No.	
				13. Type of Report and Period Covered Technical Paper	
12. Sponsoring Agency Name and Address National Aeronautics and Space Administration Washington, D.C. 20546				14. Sponsoring Agency Code	
15. Supplementary Notes					
16. Abstract <p>Anisotropic friction, deformation, and fracture studies were conducted with {0001}, {10$\bar{1}$0}, and {11$\bar{2}$0} silicon carbide surfaces in sliding contact with diamond. The experiments were conducted with loads of 0.1, 0.2, and 0.3 N at a sliding velocity of 3 mm/min in mineral oil or in dry argon at room temperature. The <1010> direction on the basal {0001} plane exhibits the lowest coefficient of friction and the greatest resistance to abrasion for silicon carbide. Anisotropic friction and deformation of the {0001}, {10$\bar{1}$0}, and {11$\bar{2}$0} silicon carbide surfaces are primarily controlled by the slip system {10$\bar{1}$0}<11$\bar{2}$0>. The anisotropic fracture during sliding on the basal plane is due to surface cracking along {10$\bar{1}$0} and sub-surface cracking along {0001}. The fracture during sliding on the {10$\bar{1}$0} and {11$\bar{2}$0} surfaces is due to surface cracking along {0001} and {11$\bar{2}$0} or {10$\bar{1}$0} and to subsurface cracking along {10$\bar{1}$0}.</p>					
17. Key Words (Suggested by Author(s)) Abrasions Surface properties Friction Wear tests Silicon carbide Fractures (materials)			18. Distribution Statement Unclassified - unlimited STAR Category 27		
19. Security Classif. (of this report) Unclassified		20. Security Classif. (of this page) Unclassified		21. No. of Pages 23	
				22. Price* A02	

